PHYSICAL REVIEW B **94**, 125118 (2016)

Interlayer electronic transport in CaMnBi$_2$ antiferromagnet

Aifeng Wang (王爱峰),[1] D. Graf,[2] Lijun Wu,[1] Kefeng Wang (王克锋),[1,*] E. Bozin,[1] Yimei Zhu,[1] and C. Petrovic[1]
[1]*Condensed Matter Physics and Materials Science Department, Brookhaven National Laboratory, Upton, New York 11973, USA*
[2]*National High Magnetic Field Laboratory, Florida State University, Tallahassee, Florida 32306-4005, USA*

(Received 7 June 2016; revised manuscript received 18 August 2016; published 12 September 2016)

We report interlayer electronic transport in CaMnBi$_2$ single crystals. Quantum oscillations and angular magnetoresistance suggest coherent electronic conduction and valley polarized conduction of Dirac states. The small cyclotron mass, high mobility of carriers, and nontrivial Berry's phase are consistent with the presence of Dirac fermions on the side wall of the warped cylindrical Fermi surface. Similarly to SrMnBi$_2$, which features an anisotropic Dirac cone, our results suggest that magnetic-field-induced changes in interlayer conduction are also present in layered bismuth-based materials with a zero-energy line in momentum space created by the staggered alkaline earth atoms.

DOI: 10.1103/PhysRevB.94.125118

I. INTRODUCTION

Similar to graphene and topological insulators, ternary AMnBi$_2$ crystals (A = alkaline earth, such as Ca, Sr, or Ba) also host quasi-two-dimensional (2D) Dirac states [1–4]. The Dirac cone in SrMnBi$_2$ is strongly anisotropic due to spin-orbit coupling, which is an essential ingredient for the magnetic valley control and valley-polarized interlayer current [5–8]. There may be multiple degenerate "valleys" (conduction-band minima) for the carriers to occupy in the electronic structure of certain crystal lattices. Such a degeneracy can be lifted in a controllable way; i.e., magnetic valley control is a degeneracy controlled by the magnetic field. The valley degree of freedom can be used to develop electronic devices [7,9]. First-principle calculations and angle-resolved photoemission (ARPES) measurements indicate that the anisotropy of the Dirac cone is determined by the local arrangement of Sr/Ca surrounding the Bi square net [5,10]. The stacking configuration of the two alkaline earth atomic layers above and below the Bi square net is different for SrMnBi$_2$ and CaMnBi$_2$, creating an anisotropic Dirac cone (SrMnBi$_2$) or a zero-energy line in momentum space (CaMnBi$_2$) [5]. Therefore, it is of interest to probe interlayer conduction in CaMnBi$_2$.

Valley control in SrMnBi$_2$ is realized through field-dependent coherent interlayer conduction, sensitive to the curvature of the side wall of the quasi-2D Fermi surface (FS) [6]. This is similar to, for example, the quasi-2D organic superconductor magnetoresistance (MR) peak structure when the magnetic field is nearly parallel to the conducting plane. The MR is explained by the open orbits or small closed orbits formed on the side of the warped FS [11]. The warped FS is easily detected by Shubnikov de Haas (SdH) oscillations since the oscillation frequency is determined by the extremal orbit [12].

In-plane electronic transport reveals that CaMnBi$_2$ is a bad metal with antiferromagnetic transition at ∼250 K, showing giant magnetoresistance [3,13,14]. The MR and quantum oscillations results indicate the existence of quasi-2D Dirac fermions in CaMnBi$_2$ [3]. Negative thermopower suggests dominant electron-type carriers, whereas the magnetic field suppresses its absolute value, consistent with the presence of Dirac fermions [15].

Here we report the angular-dependent MR and SdH in CaMnBi$_2$ when the current runs along the c axis of the crystal. The fourfold symmetry of the azimuthal angle dependence of the out-of-plane resistivity (ρ_c) indicates a valley degeneracy contribution of Dirac fermions to the interlayer conductivity. Moreover, the contribution can be lifted and controlled by the in-plane magnetic field. Compared to SrMnBi$_2$, the out-of-plane resistivity and Hall resistance suggest a larger contribution of the three-dimensional (3D) FS to the conductivity. The peak of the MR when the field is in the ab plane and the narrow angle range of the SdH indicate the existence of small closed orbits on the side of the warped FS. The SdH along the c axis features three peaks, possibly due to several extremal orbits in the α band and consistent with the angle-dependent MR results. The temperature dependence of the SdH in the ab plane reveals a small cyclotron mass, large mobility, and nozero Berry's phase in the small closed pocket. This suggests that the zero-energy line of Dirac carriers in CaMnBi$_2$ contains small closed orbits [5,10].

II. EXPERIMENTAL DETAILS

CaMnBi$_2$ single crystals were grown from high-temperature bismuth flux [3]. Neutron time-of-flight powder diffraction measurement at 300 K was performed on the POWGEN instrument, BL-11A, at the Spallation Neutron Source, Oak Ridge National Laboratory. A vanadium can containing 0.5 g of finely pulverized sample was used with an *in situ* sample changer. Powder used in the neutron experiment was obtained by pulverizing single crystals from the same batch as the single crystal used in interlayer transport experiments. The average structure was assessed through Rietveld refinements to the raw diffraction data using the GSAS operated under EXPGUI, utilizing the tetragonal space group $P4/nmm$ [16–18]. A sample for transmission electron microscopy (TEM) was prepared by crushing the single-crystal sample and then dropping it onto a Lacey carbon grid. High-resolution TEM imaging was performed using a double aberration-corrected JEOL-ARM200CF microscope with a cold-field emission gun operated at 200 kV. Single crystals

---

[*] Present address: Department of Physics, University of Maryland, College Park, Maryland 20742-4111, USA.

free of bismuth flux for magnetotransport measurements were obtained by cleaving and cutting the six faces of the cuboid. Magnetotransport measurements up to 9 T were performed using the Quantum Design PPMS-9, and those up to 35 T at the National High Magnetic Field Laboratory in Tallahassee, Florida. For the out-of-plane resistance measurement, a thick single crystal was cut to produce a needlelike sample with the long side along the *c* axis with about 5° uncertainty in order to minimize the contribution of the in-plane resistivity component. This is in contrast to the method where voltage contacts are attached on the opposite [001] planes of rectangular crystal [3,19,20]. Electrical contacts used in resistivity measurements were made for the samples using silver paste to attach Pt wires in a standard four-probe configuration. The temperature dependences of the resistivity of three independently grown crystals from the same batch were reproducible and consistent with each other. Given the sample size, the error introduced by the geometry factor can be as high as 18%.

III. RESULTS AND DISCUSSION

The $P4/nmm$ structure of $CaMnBi_2$ was confirmed through neutron powder diffraction and TEM [Figs. 1(a)–1(c)]. Neutron diffraction lattice parameters [Fig. 1(a)] are in good agreement with the reported values [21]. In addition to the main phase, about 9%, by weight, elemental Bi phase was also observed due to the small amount of Bi metal flux droplets during pulverization of the single-crystal specimen. The TEM electron diffraction pattern of $CaMnBi_2$ is also consistent with the $P4/nmm$ space group [Figs. 1(b) and 1(c)] [3].

Figure 2(a) shows the temperature dependence of the interlayer resistivity (ρ_c) for $CaMnBi_2$ measured at 0 and 9 T in the Quantum Design PPMS. The overall behavior of ρ_c is similar to that of ρ_{ab} [3,14]. Neither the anomaly corresponding to the antiferromagnetic transition at $T_N \cong 250$ K nor the broad maximum at about 170 K is observed [3,13,22]. The broad maximum in *c*-axis resistivity observed before [3] was probably introduced by the temperature gradient at the National High Magnetic Field Laboratory cryostat during the cooldown procedure. Due to antiferromagnetic order in $CaMnBi_2$, Mn-related bands are well spin polarized and separated away from the Fermi level; consequently, the electronic transport properties of $CaMnBi_2$ are dominated by the anisotropic Dirac cone formed by the Bi *p* band [5]. The origin of the resistivity anomaly at $T_0 = 50$ K has been attributed to weak ferromagnetic order or spin reorientation [3,14]. However, this anomaly does not stem from the change in the average crystal structure since there is a smooth evolution of lattice parameters of the *P4/nmm* space group from 310 K to $T = 10$ K upon cooling [22]. Compared to the ρ_c of $SrMnBi_2$, the hump around 200 K is very weak [1], indicating that the FS is more 3D than that in $SrMnBi_2$. The magnetoresistance $MR = [\rho_c(B) - \rho_c(0)]/\rho_c(0)]$ is about 10% above 50 K in a 9-T field but increases strongly below 50 K, to 44% at 2 K, similarly to the in-plane MR of $CaMnBi_2$. The slope of the Hall resistance $R_{xy}(B)$ changes from positive to negative at ~16 T [Fig. 2(a), inset], suggesting the presence of multiple bands in the electronic transport. According to the classical expression for the Hall coefficient when both electron- and hole-type carriers are present [23],

$$\frac{\rho_{xy}}{\mu_0 H} = R_H = \frac{1}{e}\frac{\left(\mu_h^2 n_h - \mu_e^2 n_e\right) + (\mu_h \mu_e)^2(\mu_0 H)^2(n_h - n_e)}{(\mu_e n_h + \mu_h n_e)^2 + (\mu_h \mu_e)^2(\mu_0 H)^2(n_h - n_e)^2}.$$

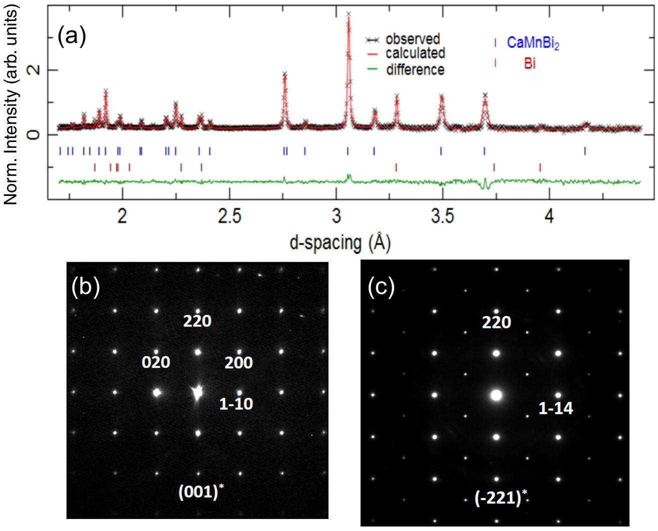

FIG. 1. (a) Structural refinement of neutron powder diffraction data on $CaMnBi_2$ at 300 K. Electron diffraction pattern of $CaMnBi_2$ viewed along (b) the [001] and (c) the [−221] directions. Reflection conditions can be derived from (b) as $h + k = 2n$ (*n* is an integer) for *hk*0, consistent with the reflection condition of the $P4/nmm$ space group.

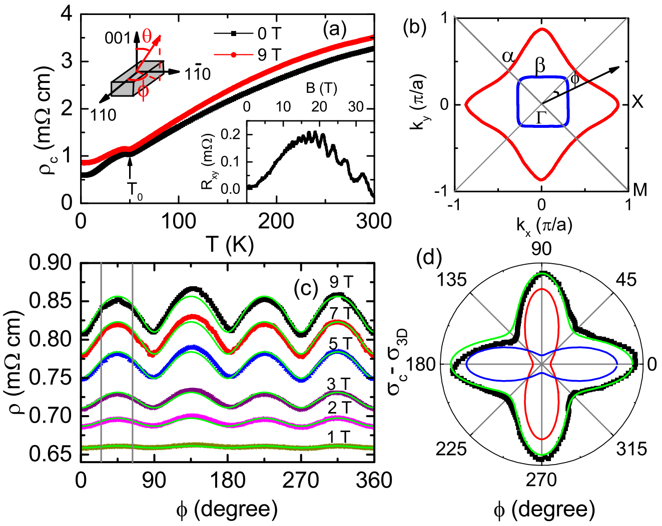

FIG. 2. (a) Temperature dependence of the out-of-plane resistivity of $CaMnBi_2$ in the $B = 0$ T and $B = 9$ T magnetic fields. The scheme shows how the polar (θ) and azimuthal (ϕ) are determined. Inset: MR of $CaMnBi_2$. (b) Fermi surface of $CaMnBi_2$ obtained by ARPES measurements [10]. The orientations of the Fermi pocket with respect to the crystal axes are also shown. (c) Azimuthal angle (ϕ) dependence of the out-of-plane resistivity at $T = 2$ K under different magnetic fields. Green lines represent fits using the three-parameter equation (see text). (d) Polar plot of $\sigma_c - \sigma_{3D}$ (black squares) and the three-parameter fit (green line); red and blue lines represent the contributions of valleys with odd and even indexes, respectively.

In the weak-field limit, the equation can be simplified as $R_H = e^{-1}(\mu_h^2 n_h - \mu_e^2 n_e)/(\mu_h n_h + \mu_e n_e)^2$, whereas $R_H = 1/(n_h - n_e)e$ in the high-field limit. If $\mu_h < \mu_e$, a change in the slope indicates that the dominant carriers in CaMnBi$_2$ are holes at low field and electrons at high field. This is different from SrMnBi$_2$, where the Hall resistance slope remains negative up to 60 T [1]. The interlayer resistivity and Hall resistance suggest that the transport of CaMnBi$_2$ is dominated by a 3D hole Fermi pocket at the Brillouin zone center and that the FS is more 3D when compared to that of SrMnBi$_2$.

The Fermi surfaces of CaMnBi$_2$ and SrMnBi$_2$ both have a holelike square-shaped part around the Γ point. Differently from the four small isolated FSs in the Γ-M direction in SrMnBi$_2$, there is a large diamondlike FS connecting four equivalent X points in the first Brillouin zone [10], as shown in Fig. 2(b). The similarity of CaMnBi$_2$ and SrMnBi$_2$ FSs indicates that valley-polarized interlayer conduction is possible in CaMnBi$_2$.

For a twofold anisotropic Fermi pocket and when the field is applied along the shorter axis, the electrons on the flat part of the FS experience nearly zero Lorentz force, whereas Lorentz force makes the electrons on the side wall move along the closed orbits. This leads to minima in ρ_c. Therefore, the magnetic field can be an effective tool to control the valley contribution to the out-of-plane resistivity [6,7]. The azimuthal angle (ϕ) dependence of ρ_c exhibits strong fourfold symmetry due to the different contribution of the valleys controlled by the in-plane field orientation. For a quasi-2D FS, $\rho_c(\phi)$ can be fitted with an empirical model; we assume that the holelike β FS has a negligible ϕ dependence, while the four α FSs are ellipsoid, with the long axis perpendicular to the Γ-M line. Therefore, $\sigma_c(\phi) \approx 1/\rho_c(\phi)$ can be described by the formula [6]

$$\begin{aligned}\sigma_c(\phi) &= \sum_{n=1}^{4} \sigma_{\alpha,n}(\phi) + \sigma_\beta \\ &= \frac{2\,\sigma_{2\mathrm{D}}}{1+r\cos^2\phi} + \frac{2\,\sigma_{2\mathrm{D}}}{1+r\cos^2(\phi+\pi/2)} + \sigma_{3\mathrm{D}}\,,\end{aligned}$$

where $\sigma_{2\mathrm{D}}$ and $\sigma_{3\mathrm{D}}$ are the contributions of the α and β FSs, respectively. The parameter r is a measure of the anisotropy of magnetoconductivity. As shown in Fig. 2(c), all curves can be fitted with this empirical formula: $\sigma_{2\mathrm{D}} = 0.06\ (\mathrm{m}\Omega\,\mathrm{cm})^{-1}$, $\sigma_{3\mathrm{D}} = 1.09\ (\mathrm{m}\Omega\,\mathrm{cm})^{-1}$, and $r = 4.28$ can be obtained from the fitting of $\rho_c(\phi)$ at 9 T, and the contribution of the quasi-2D FS to $\sigma_{2\mathrm{D}} - \sigma_{3\mathrm{D}}$ is illustrated in Fig. 2(d). The ratio between the quasi-2D (four α bands) and the 3D (β band) conductivities $4\sigma_{2\mathrm{D}}/\sigma_{3\mathrm{D}} \sim 0.22$, indicating that $\rho_c(\phi)$ is dominated by the 3D holelike β FS. The quasi-2D electronlike α bands contribute only about ∼22% of the total out-of-plane conductivity, consistent with the small quasi-2D FSs observed by ARPES and quantum oscillations [3,10].

We note that the fourfold symmetry is broken at a high magnetic field [Fig. 2(c)] into twofold symmetry. The ρ_c value at $\pi/2$ and $3\pi/2$ is larger than those at $\pi/4$ and $3\pi/4$. A similar result has been observed for SrMnBi$_2$ and Bi, possibly due to the formation of nematic liquid of electrons [1,7,24].

Figure 3 shows the polar angle (θ) dependence of ρ_c at various azimuthal angles (ϕ). Magnetotransport of solids is governed by the extremal cross section S_F of the FS; as a result, $S_F(\theta) = S_0/|\cos(\theta)|$ is expected for a 2D FS. The $\rho_c(\theta)$ exhibits twofold symmetry at low temperatures and high fields and can be fitted by $|\cos(\theta)|$, consistent with the quasi-2D FS in CaMnBi$_2$. There are two shoulders around $\theta = 90^o$, where the field is parallel to the ab plane. The shoulder location (Yamaji) angles are magnetoresistance maxima where the carriers in the warped cylindrical FS behave as in a 2D electronic system [25].

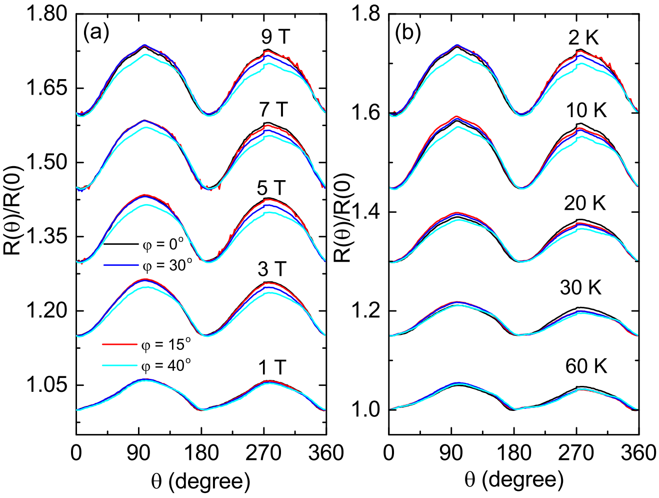

FIG. 3. (a) Normalized resistivity $\rho_c(\theta)/\rho_c(0)$ taken at 2 K for different azimuthal angles (ϕ) and in different fields. (b) Normalized resistivity $\rho_c(\theta)/\rho_c(0)$ taken at 9 T with varying ϕ and temperature. (a) and (b) have the same legend. Each subsequent data set is shifted upward by 0.15 for clarity.

The $\rho_c(\theta)$ measured in a high field is presented in Fig. 4(a). It shows a peak at around 90°, which can be attributed to self-crossing orbits or closed orbits that appear on the side of the warped FS [6,11]. Moreover, the peak width is independent of the field strength, as shown in the inset in Fig. 4(a). In the case of self-crossing orbits, the angular width of the peak should be inversely proportional to the magnetic field. Thus, the peak at $\theta = 90°$ can be ascribed to closed orbits on the side of the cylindrical FS [11]. The series of peaks between 120° and 180° are due to Yamaji oscillations [11]. Our results indicate coherent interlayer conduction at low temperatures and the presence of the quasi-2D FS in CaMnBi$_2$, in agreement with the previous report [3].

Figure 4(b) shows the magnetic field dependence of ρ_c up to 35 T. No oscillation is observed below 10 T, indicating the absence of Bi flux in the MR signal since elemental bismuth shows quantum oscillations at very low magnetic fields [26]. The MR decreases with the increased angle. The slopes of the MRs decrease considerably at around 3 T. The resistance exhibits linear-in-field dependence at high magnetic fields. No transition corresponding to the magnetic order change is observed in the resistivity at high magnetic fields. Nonsaturating linear MR has been reported in several complex materials like Ag$_{2+\delta}$Se, SrMnBi$_2$, and BaFe$_2$As$_2$ [1,27,28]. Linear MR can be observed when Dirac electrons condense at the lowest Landau level (LL) [29,30]. This is easily realized in modest magnetic fields since the distance between the lowest LL and the first LLs of Dirac-like fermions in a magnetic field is large, in contrast to the conventional paraboliclike energy dispersion [28,29,31,32]. Whereas linear MR is also observed in simple metals, such as potassium [33], in-plane

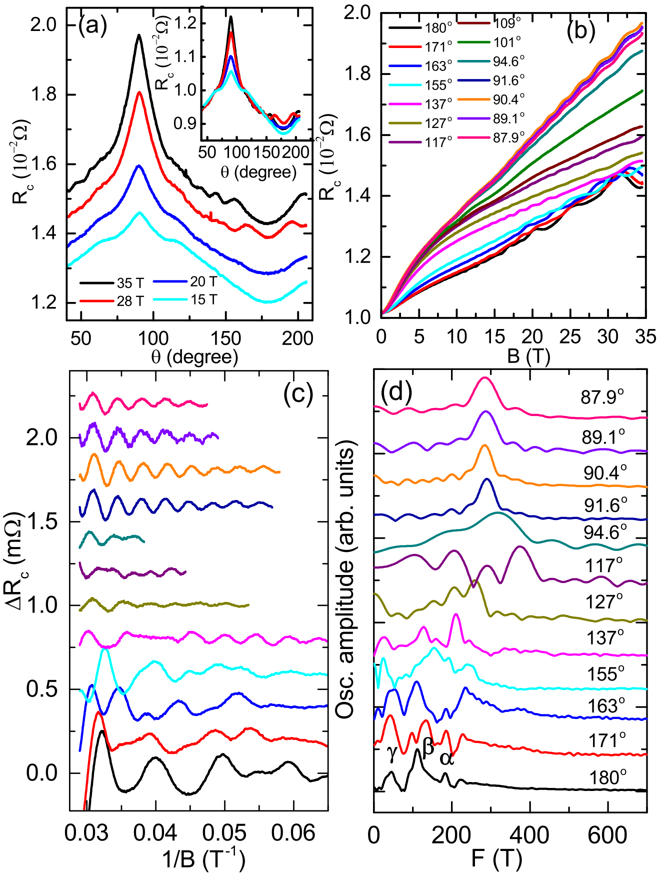

FIG. 4. (a) Angle dependence of the out-of-plane resistance $R_c(\theta)$ taken at 2 K in magnetic fields up to 35 T. Inset: $R_c(\theta)$ of CaMnBi$_2$ normalized to $R_c(114^\circ)$. (b) Magnetic-field dependence of the out-of-plane resistance R_c up to 35 T for CaMnBi$_2$. (c) SdH oscillation component $\Delta R_c = R_c - \langle R_c \rangle$ vs $1/B$ for different angles measured up to 35 T at 0.7 K. (d) FFT spectra of the SdH oscillations corresponding to the oscillation component in (c). (c) and (d) have the same legend.

MR, quantum oscillations, thermal transport, ARPES studies, and first-principle calculations strongly suggest the presence of Dirac states in CaMnBi$_2$ [3,5,10,15].

Shubnikov–de Haas (SdH) oscillations are observed in the c-axis electronic transport [Figs. 4(b)–4(d)]. At first, the oscillation magnitude decreases very quickly with the angle increase, and the oscillation disappears at $\theta = 101^\text{o}$. The oscillation appears again with further angle decrease. Hence, clear oscillation can be observed when the field is either along the c axis [3,14] or in the ab plane (this study). A 3D FS would produce oscillations for all directions of the magnetic field; therefore it is unlikely in CaMnBi$_2$ due to the absence of oscillation at 101°. Another possibility is that the oscillation is due to the Fermi-surface topological effect, where small closed orbits appear on the side of the warped cylindrical FS. This model can also interpret the absence of oscillations at 101° and the presence of the oscillations only in a narrow range around 90°, in agreement with $\rho_c(\theta)$. As shown in the calculated Fermi surfaces of CaMnBi$_2$ in Fig. 4 in Ref. [5], this closed orbit is very likely located on the convex part of the electron Fermi pocket. A schematic of the closed orbits is given in Fig. 3(c) of Ref. [6].

In Fig. 4(c), we show the oscillatory component of ΔR_c versus $1/B$ for different angles after subtracting the smooth background. The oscillation component shows periodic behavior in $1/B$. We perform fast Fourier transform (FFT) on the oscillation component in Fig. 4(c); the results are presented in Fig. 4(d). There is only one frequency, $F = 286$ T, at which the field is parallel to the ab plane. When the field is applied along the c axis, three FFT peaks are observed. The peaks are located at 45.4, 111.8, and 184.0 T, and the corresponding FS cross sections are 0.43, 1.07, and 1.76 nm^{-2} according to the Onsager relation $F = (\Phi_0/2\pi^2)A_F$, where Φ_0 is the quantum flux and A_F is the cross-sectional area of the FS. All three Fermi pockets are very small, only about 0.2%, 0.5%, and 0.9% of the total area of the Brillouin zone. $F = 184$ T is very close to the dominant frequency observed before, therefore it can be assigned to an α band with a Dirac point [3,14]. Other frequencies could come from the α band, which is a warped cylindrical Fermi pocket with several extremal orbits. This is consistent with the closed orbits observed on the side wall of the cylindrical Fermi pocket. The oscillations show multiband behavior when the fields tilt from the c axis. In what follows we discuss the SdH when the field is applied parallel to ab plane [Figs. 5(a)–5(d)].

Temperature dependence of quantum oscillations is shown in Fig. 5(a) and Fig. 5(b). Semiclassically, the SdH oscillation can be described by

$$\Delta\rho \propto R_T R_D \cos\left[2\pi\left(F/B + \tfrac{1}{2} + \beta\right)\right],$$

where $R_T = \frac{\alpha m^* T}{B\sinh(\alpha m^* T/B)}$ is the thermal damping factor, and $R_D = \exp(-\alpha m^* T_D/B)$ is the Dingle damping factor, in which $\alpha = 14.69$ T/K. $2\pi\beta$ is Berry's phase. The thermal damping factor can be used to determine the cyclotron effective mass from the Lifshitz-Kosevitch formula. As shown in Fig. 5(c), fitting of the amplitude gives the cyclotron mass $m^* \approx 0.53$, heavier compared to the values of 0.35 obtained from in-plane oscillation of CaMnBi$_2$ and 0.29 in SrMnBi$_2$ [1,3]. The Dingle temperature $T_D = 8.23$ K can be obtained from the Dingle plot in Fig. 5(c). Therefore, a scattering time of $\tau_q = 1.47 \times 10^{-13}$ s can be obtained by $T_D = \frac{\hbar}{2\pi k_B \tau_q}$. Then the mobility $\mu_q = e\tau_q/m_c$ is 488 cm^2 V^{-1} s^{-1}. The scattering time and mobility are even higher than in SrMnBi$_2$ and Cd$_3$As$_2$, typical Dirac materials, consistent with the presence of Dirac fermions in this Fermi pocket [1,34].

The Fourier transform spectrum of the oscillation at 0.7 K reveals a periodic behavior in $1/B$ with a frequency $F = 299$ T. The oscillation frequency determined by the slope of the linear fit of the Landau index is 299 T, in agreement with the FFT results. The FS cross section normal to the field is $A_F = 2.86$ nm^{-2}, and $k_F = 9.54 \times 10^8$ m^{-1} can be obtained. Therefore, the Fermi velocity $v_F = \hbar k_F/m^* = 2.08 \times 10^5$ m/s and the Fermi energy $E_F = 130$ meV. The mean free path is estimated to be by $l = v_F\tau = 30.6$ nm.

SdH oscillations in metals are related to successive emptying of the LL in the magnetic field whereas the LL index n is correlated with the cross section of the FS S_F as

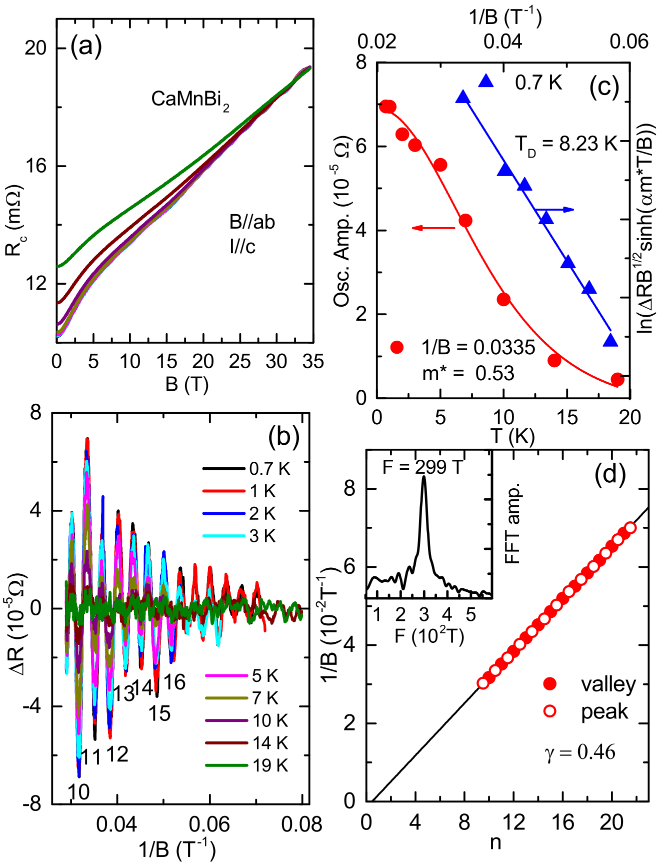

FIG. 5. (a) Magnetic-field dependence of the resistance of CaMnBi$_2$ measured at various temperatures up to 19 K. (b) The oscillatory component as a function of $1/B$. Integer indices of the Landau levels. (a) and (b) have the same legend. (c) Left: Temperature dependence of the oscillation amplitude at different fields. Solid lines are the fits by the Lifshitz-Kosevitch formula. Right: Dingle plot at 0.7 and 1 K. (d) Landau index plots n vs $1/B$ at 0.7 K. Inset: FFT spectra at 0.7 K.

$2\pi(n+\gamma) = S_F(\hbar/eB)$. In the Landau fan diagram [Fig. 5(d)] the peaks and valleys fall on a straight line. The linear fit gives $\gamma \cong 0.46$; γ should be 0 for conventional metals but is $\pm 1/2$ for Dirac fermions due to the nontrivial Berry's phase. The $\gamma \sim 1/2$ and high Fermi velocity confirm the existence of Dirac fermions at the orbits on the side of the warped cylindrical FS. The Dirac Fermion with large Fermi velocity on the side wall of the Fermi cylinder have important effect on the ρ_c which could explain why ρ_c does not show clear ϕ dependence.

IV. CONCLUSIONS

In conclusion, we studied the angle-dependent out-of-plane magnetotransport in CaMnBi$_2$. ρ_{xy} and out-of-plane ρ_{xx} indicate that the FS is more 3D when compared to SrMnBi$_2$. The interlayer conduction depends on the orientation of in-plane magnetic field. This suggests that the valley-polarized interlayer current through magnetic valley control can be realized in CaMnBi$_2$. The angular dependence of MR and the SdH show that the the closed orbits appear on the side of the warped cylindrical FS. Small FS, small cyclotron mass, large mobility, and nonzero Berry phase are consistent with the existence of Dirac fermions on the Fermi pocket on the side wall of the warped cylindrical FS.

ACKNOWLEDGMENTS

Work at BNL was supported by the U.S. DOE-BES, Division of Materials Science and Engineering, under Contract No. DE-SC0012704. The experiment at ORNL Spallation Neutron Source was sponsored by the Scientific User Facilities Division, BES, U.S. DOE. Work at the National High Magnetic Field Laboratory was supported by the NSF Cooperative Agreement No. DMR-0654118 and by the state of Florida.

[1] J. Park, G. Lee, F. Wolff-Fabris, Y. Y. Koh, M. J. Eom, Y. K. Kim, M. A. Farhan, Y. J. Jo, C. Kim, J. H. Shim, and J. S. Kim, Phys. Rev. Lett. **107**, 126402 (2011).
[2] K. Wang, D. Graf, H. Lei, S. W. Tozer, and C. Petrovic, Phys. Rev. B **84**, 220401(R) (2011).
[3] K. Wang, D. Graf, L. Wang, H. Lei, S. W. Tozer, and C. Petrovic, Phys. Rev. B **85**, 041101(R) (2012).
[4] L. Li, K. Wang, D. Graf, L. Wang, A. Wang, and C. Petrovic, Phys. Rev. B **93**, 115141 (2016).
[5] G. Lee, M. A. Farhan, J. S. Kim, and J. H. Shim, Phys. Rev. B **87**, 245104 (2013).
[6] Y. J. Jo, J. Park, G. Lee, M. J. Eom, E. S. Choi, J. H. Shim, W. Kang, and J. S. Kim, Phys. Rev. Lett. **113**, 156602 (2014).
[7] Z. Zhu, A. Collaudin, B. Fauqué, W. Kang, and K. Behnia, Nat. Phys. **8**, 89 (2012).
[8] R. Küchler, L. Steinke, R. Daou, M. Brando, K. Behnia, and F. Steglich, Nat. Mater. **13**, 461 (2014).
[9] D. Xiao, W. Yao, and Q. Niu, Phys. Rev. Lett. **99**, 236809 (2007).
[10] Y. Feng, Z. Wang, C. Chen, Y. Shi, Z. Xie, H. Yi, A. Liang, S. He, J. He, Y. Peng, X. Liu, Y. Liu, L. Zhao, G. Liu, X. Dong, J. Zhang, C. Chen, Z. Xu, X. Dai, Z. Fang, and X. J. Zhou, Sci. Rep. **4**, 5385 (2014).
[11] N. Hanasaki, S. Kagoshima, T. Hasegawa, T. Osada, and N. Miura, Phys. Rev. B **57**, 1336 (1998).
[12] D. Shoeneberg, *Magnetic Oscillation in Metals* (Cambridge University Press, Cambridge, UK, 1984).
[13] J. K. Wang, L. L. Zhao, Q. Yin, G. Kotliar, M. S. Kim, M. C. Aronson, and E. Morosan, Phys. Rev. B **84**, 064428 (2011).
[14] J. B. He, D. M. Wang, and G. F. Chen, Appl. Phys. Lett. **100**, 112405 (2012).
[15] K. Wang, L. Wang, and C. Petrovic, Appl. Phys. Lett. **100**, 112111 (2012).
[16] H. M. Rietveld, Acta Crystallogr. **22**, 151 (1967).
[17] A. C. Larson and R. B. von Dreele, Report No. LAUR-86-748, Los Alamos National Laboratory, Los Alamos, NM, 1987.
[18] B. H. Toby, J. Appl. Crystalogr. **34**, 210 (2001).

[19] X. F. Wang, T. Wu, G. Wu, H. Chen, Y. L. Xie, J. J. Ying, Y. J. Yan, R. H. Liu, and X. H. Chen, Phys. Rev. Lett. **102**, 117005 (2009).

[20] J. Edwards and R. F. Frindt, J. Phys. Chem. Solids **32**, 2217 (1971).

[21] E. Brochtel, G. Cordier, and H. Shäfer, Z. Naturforsch. b **35**, 1 (1980).

[22] Y. F. Guo, A. J. Princep, X. Zhang, P. Manuel, D. Khalyavin, I. I. Mazin, Y. G. Shi, and A. T. Boothroyd, Phys. Rev. B **90**, 075120 (2014).

[23] P. B. Allen, in *Handbook of Superconductivity*, edited by C. P. Poole, Jr. (Academic Press, New York, 1999), p. 478.

[24] E. Fradkin, S. A. Kivelson, M. J. Lawler, J. P. Eisenstein, and A. P. Mackenzie, Annu. Rev. Condens. Matter Phys. **1**, 153 (2010).

[25] E. Ohmichi, Y. Maeno, and T. Ishiguro, J. Phys. Soc. Jpn. **68**, 24 (1999).

[26] V. S. Edelman, Adv. Phys. **25**, 555 (1976).

[27] R. Xu, A. Husmann, T. F. Rosenbaum, M.-L. Saboungi, J. E. Enderby, and P. B. Littlewood, Nature **390**, 57 (1997).

[28] K. K. Huynh, Y. Tanabe, and K. Tanigaki, Phys. Rev. Lett. **106**, 217004 (2011).

[29] A. A. Abrikosov, *Fundamentals of the Theory of Metals* (North-Holland, Amsterdam, 1988).

[30] A. A. Abrikosov, Europhys. Lett. **49**, 789 (2000).

[31] Y. Zhang, Z. Jiang, Y.-W. Tan, H. L. Stormer, and P. Kim, Nature (London) **438**, 201 (2005).

[32] D. Miller, K. Kubista, G. Rutter, M. Ruan, W. de Heer, P. First, and J. Stroscio, Science **324**, 924 (2009).

[33] J. R. Reitz and A. W. Overhauser, Phys. Rev. **171**, 749 (1968).

[34] T. Liang, Q. Gibson, M. N. Ali, M. H. Liu, R. J. Cava, and N. P. Ong, Nat. Mater. **14**, 280 (2015).